

Facile Preparation of Large-Area, Ultrathin, Flexible Semi-Transparent Perovskite Solar Cells via Spin-Coating

Łukasz Przypis^{1,2}, Wiktor Żuraw^{1,2}, Miłosz Grodzicki¹, Mateusz Ścigaj², Robert Kudrawiec¹, and Artur P Herman¹

¹Department of Semiconductor Materials Engineering, Wrocław University of Science and Technology

²Saule Research Institute

March 04, 2024

Abstract

The development of emerging photovoltaic technology has promoted the innovation of building-integrated photovoltaics (BIPV), not only in lower cost and simpler processing technology but also in a variety of additional features, such as flexibility and transparency. Semi-transparent solar cells that allow partial transmission of visible light are excellent candidates for BIPVs owing to their unique properties and potential for integrated energy solutions. In this work, we present a straightforward and highly reproducible protocol for depositing extremely uniform and ultra-thin perovskite layers. Our solution-processed perovskite solar cells, fabricated on flexible polymer 2 substrates with large active area (1 cm²), achieved a noteworthy 5.7% power conversion efficiency (PCE) under standard conditions (AM 1.5G radiation, 100 mW cm⁻²) accompanied by an Average Visible Transmittance (AVT) of 21.5% for full device architecture with 10 nm thick silver electrode. We present a simple yet elegant fabrication procedure for semi-transparent perovskite solar cells without any additional antireflective layers. Furthermore, we fabricated working perovskite solar cells with the thinnest active layer of spin-coated MAPbI₃ reported so far (10 nm) exhibiting 1.9% PCE and 41.1% AVT (62.9% AVT without electrode). These results hold great promise for the integration of perovskite-based semi-transparent solar cells into real-world applications, advancing the landscape of renewable energy.

Facile Preparation of Large-Area, Ultrathin, Flexible Semi-Transparent Perovskite Solar Cells via Spin- Coating

Łukasz Przypis^{1,2}, ‡ Wiktor Żuraw^{1,2}, ‡ Miłosz Grodzicki¹, Mateusz Ścigaj², Robert Kudrawiec¹,
Artur P. Herman¹*

¹Department of Semiconductor Materials Engineering, Wrocław University of Science and
Technology, Wybrzeże Wyspiańskiego 27, 50-370 Wrocław, Poland

²Saule Research Institute, Dunska 11, 54-427 Wrocław, Poland

KEYWORDS semi-transparent solar cells, flexible solar cells, metal halide perovskites, spin-coating, methylammonium lead iodide

The development of emerging photovoltaic technology has promoted the innovation of building-integrated photovoltaics (BIPV), not only in lower cost and simpler processing technology but also in a variety of additional features, such as flexibility and transparency. Semi-transparent solar cells that allow partial transmission of visible light are excellent candidates for BIPVs owing to their unique properties and potential for integrated energy solutions. In this work, we present a straightforward and highly reproducible protocol for depositing extremely uniform and ultra-thin perovskite layers. Our solution-processed perovskite solar cells, fabricated on flexible polymer

substrates with large active area (1 cm²), achieved a noteworthy 5.7% power conversion efficiency (PCE) under standard conditions (AM 1.5G radiation, 100 mW cm⁻²) accompanied by an Average Visible Transmittance (AVT) of 21.5% for full device architecture with 10 nm thick silver electrode. We present a simple yet elegant fabrication procedure for semi-transparent perovskite solar cells without any additional antireflective layers. Furthermore, we fabricated working perovskite solar cells with the thinnest active layer of spin-coated MAPbI₃ reported so far (10 nm) exhibiting 1.9% PCE and 41.1% AVT (62.9% AVT without electrode). These results hold great promise for the integration of perovskite-based semi-transparent solar cells into real-world applications, advancing the landscape of renewable energy.

INTRODUCTION

Metal halide perovskites (MHPs) and in particular hybrid organic inorganic perovskites (HOIPs) appear as a truly game-changing family of materials for energy conversion due to the unique combination of optoelectronic properties and relatively facile fabrication processes, which have contributed to their widespread exploration as a potential alternative to conventional solar cell technologies.¹⁻⁵ Perovskite solar cells (PSCs) are by far the most efficient solution-processable solar cells, with a record power conversion efficiency (PCE) of 25.7% for single-junction opaque solar cells.⁶ One area of particular interest within the field of MHP-based optoelectronic devices is the development of semi-transparent ultrathin solar cells. The integration of semi-transparent perovskite layers in solar cells offers exciting opportunities for applications such as building-integrated photovoltaics (BIPV).⁷ Semi-transparent photovoltaic technology not only generates power but also contributes to creating a comfortable natural living environment. Allowing natural light to enter the building, it simultaneously reduces the energy consumption. Additionally, it can control the spread of heat, providing both temperature and visual comfort.⁸⁻¹⁰ In addition to the

high PCE, the PSCs have a good application prospect in the field of semi-transparent photovoltaic devices owing to the high absorption coefficient and the low-temperature preparation processes.¹¹

The quest for semi-transparent perovskite layers involves overcoming several technical challenges. One of the primary concerns is to maintain uniform ultrathin film coverage while minimizing the occurrence of pinholes and voids, which is critical for attaining high-quality perovskite layers. Insufficient reproducibility and homogeneity result in a spread of performance in the resulting photovoltaic devices. Semi-transparent perovskite films can be obtained using diverse well-established deposition techniques such as: spin-coating,¹² blade-coating,¹³ and dip-coating.¹⁴ These methods are very convenient considering further scaling-up, however, thickness control within the crucial for transparency sub-100 nm range is significantly limited.¹⁵ Therefore, new approaches to overcoming these obstacles have been developed.

First, the so-called spontaneous dewetting, which employs the treatment of as-prepared perovskite thin film with low-vapor-pressure solvent.¹⁶ This method results in an archipelago-like microstructure (randomly grown perovskite islands) of active layer providing the neutral color of full devices. Another alternative is mesh-assisted deposition which leads to a similar microstructure with partial coverage of the perovskite film on the substrate which is achieved by controlled growth in a grid structure.^{16–19} The major disadvantage of these two methods, putting aside the additional processing step is that electron and hole-transporting materials (ETM and HTM respectively) are in direct contact. Quite recently preparation of conformal perovskite 10 nm layer using vacuum evaporation has been reported.²⁰ Despite promising results, the entire fabrication process is much more complex, though, and therefore more challenging for scaling up. Hence, the preparation of sub-100 nm perovskite films with a conformal profile in the wet process is still a challenge. In **Table 1**, we provide a summary that compares our results to previously

reported solution-processed and thermally evaporated semi-transparent perovskite devices.²¹⁻²⁵ Here it is worth to note that taking into account active area and flexible substrate our results are unprecedented in terms of PCE and AVT. Furthermore one should note that considering real-world applications and technological significance our process is the only one which does not require vacuum evaporation or specially prepared substrate.

Table 1. Characteristics of semi-transparent PSCs with active layer thickness below 100 nm.

ACTIVE AREA	DEVICE ARCHITECTURE	THICKNESS	PCE	AVT [%], SPECTRAL RANGE	REF.
Glass 0.06 cm ²	FTO/c-TiO ₂ /AAO(honeycomb shaped scaffold)+ MAPbI _{3-x} Cl _x /Spiro-OMeTAD/MoO _x /ITO	90 nm ^a	8.50%	43, 400-800	21
Glass, 0.16 cm ²	FTO/c-TiO ₂ /MAPbI ₃ / Spiro- OMeTAD/MoO _x /Au/MoO _x	54 nm ^a	5.30%	31, 370-740	22
Glass 0.06 cm ²	ITO/PTAA/ Cs _{0.1} FA _x PbI _{2+x} Br _{0.1} /PCBM/BCP/Al/Ag	50 nm ^b	6.93%	31,-	23
Flex 0.08 cm ²	ITO/MoO _x /TaTm/MAPbI ₃ /C ₆₀ /BCP/Cu/Ag	50 nm ^b	4.03%	19,-	24
Glass 0.12 cm ²	ITO/PEDOT:PSS/MAPbI ₃ /PCBM/Au/LiF	40 nm ^b	3.40%	35, 400-800	25
Glass 0.05 cm ²	ITO/PTAA/PEA-CsPbI ₃ /PCBM/BCP/Al/Ag	10 nm ^b	3.60%	54, -	23
This work:					
Flex 1.00 cm ²	IZO/PEDOT:PSS/MAPbI ₃ /C ₆₀ /BCP/Ag	30 nm ^a	5.70%	21.5, 300- 900	
Flex 1.00 cm ²	IZO/PEDOT:PSS/MAPbI ₃ /C ₆₀ /BCP/Ag	10 nm ^a	1.90%	41.1, 300- 900	

^aspin-coated, ^bvacuum deposited perovskite layer

Understanding the formation mechanism of solid perovskite film from precursor solution is one of the fundamental rules for preparation of high-quality perovskite films. However, few studies have focused on the effect of colloidal characteristics on the formation of perovskite films. In our work, we deem that high-quality spin-coated ultrathin perovskite films can be obtained by

designing and controlling the colloidal characteristics of the perovskite precursor. A comprehensive understanding of precursor solution impurities on the material properties is essential for the improvement of photovoltaic performance. It directly impacts thin film quality and device performance. Precursor purity in solution is also considered to affect the characteristics of the perovskite films such as crystal growth, charge carrier recombination dynamics, and electron/hole diffusion length.²⁶ Even common methods, like raw material mixing, can yield lead polyhalide coordination complexes. Solvent molecules may compete as ligands for Pb^{2+} . The presence of these complexes, intermediate phases, or impurities hampers nucleation and crystal growth, affecting physiochemical properties and reproducibility. Precursor ink, typically colloidal, depends on particle-solvent interactions. The size and concentration of colloids affect film quality and morphology. Lead polyhalide networks in the solution impact crystallization rate and final properties. Colloid formation/stabilization is influenced by precursor purity. Defects and grain boundaries cause performance losses.

Importantly, our objective was not to optimize the device structure for the best performance or PL emission. Instead, our aim was to demonstrate that using simple processing, i.e. spin-coating of an ultra-thin perovskite layer by one-step methodology, we are still able to obtain good performance with high transparency of PSCs on large-area flexible substrates. We are convinced that our methodology is not limited solely to spin-coating but it holds great promise for other wet fabrication methods of PSCs such as blade-coating or slot-die-coating as they also rely on ink chemistry.

RESULTS AND DISCUSSION

Keeping in mind all the complexities related to the precursor ink composition we decided to follow the quote ‘simplicity is the keynote of all true elegance’ by Coco Chanel, i.e. we used

highly pure raw materials without additives. To avoid the use of hydroiodic acid and accompanying hypophosphorous acid (HPA) stabilizer, we synthesized MAI using molecular iodine as a halide source, which was subsequently reduced in situ by formic acid, resulting in the production of highly pure methylammonium iodide.²⁷ Furthermore, this method enables effective purification of MAI, particularly from residual iodine, which contributes to its exceptional stability without the requirement for external stabilizers, as evidenced in **Figure S3** and **Figure S4**. Additional discussion on the precursor ink chemistry is detailed in the **Supplementary Information**. Although in this work we used freshly synthesized MAI, in **Figure S1** two years old MAI without any evidence of aging is presented (i.e. no yellowing which originates from the presence of free-iodine can be observed). As a lead source, we used commercial PbI_2 of high purity (see Figure S2). The inks were prepared by dissolving precursors in DMF:DMSO mixture (9.0:1.1, v/v). The resulting dispersion was stirred for 2 h at room temperature to get the transparent inks.

Firstly, we started the characterization of the prepared perovskite precursor solution by the rheological properties of the perovskite precursor solution. We measured the dynamic light scattering (DLS). The perovskite precursor inks prepared by our strategy demonstrated a narrow size distribution of colloidal particles with a distribution around 100 nm (**Figure 1a**). The presence of a small and narrowly distributed particle size is beneficial for the creation of dense and compact packed grain structures in the resulting films.^{28,29} Additionally, it's noteworthy that the elimination of larger micrometer-sized particle distribution is accomplished through the use of ultra-pure precursors.

Plausible, in our philosophy, using ultra-pure methylammonium iodide and lead iodide, the solvation of perovskite precursors in the DMF/DMSO solvent system was systematic. Colloidal nuclei were well-formed, and the dissolution of the precursor went at a similar rate. Finally, a

narrow size distribution of the particles in the solution was obtained. These nanosized particles are not likely iodoplumbate complexes but are probably perovskite-solvent complexes like the intermediate phase. In contrast, in the typical MAPbI₃ precursor ink, the formation of the colloid may be affected by insoluble impurities, which introduce the seeds leading to the growth of bigger particles. Furthermore, we conducted an investigation into the stability of our inks over time, performing DLS measurements after 48 hours and 7 days. Impressively, our inks exhibited remarkable stability over time, showing no signs of particle aggregation (**Figure 1b**). For the investigation of the chemistry of precursor solutions, MAPbI₃ inks with various concentrations at RT were studied using FTIR spectroscopy. It can be clearly seen in **Figure 1c** that the position of bands is independent of the concentration of perovskite.

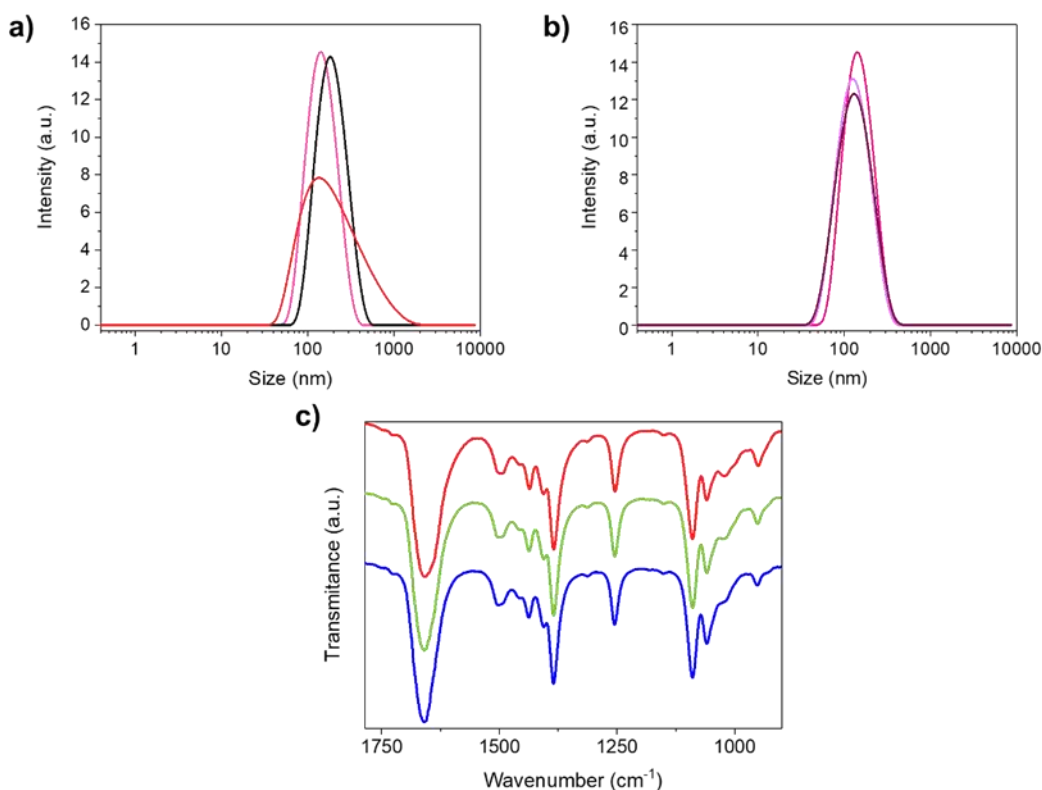


Figure 1. **a)** Colloidal properties of perovskite precursors at room temperature - size distribution by dynamic light scattering for fresh inks: black – 0.085M, pink – 0.050M, red – 0.037M ; **b)** aged ink 0.050M: pink – fresh, magenta – 48h, ruby – 7 days ; **c)** FTIR spectra of perovskite precursors with different concentrations: blue – 1.00M, green – 0.050M, re – 0.037M.

The following spectral features for each ink can be distinguished; S–O and C–S stretching vibrations related to interactions of DMSO with Pb^{2+} at $\sim 1,000\text{ cm}^{-1}$; N–H stretching in the range between $3,200$ and $3,450\text{ cm}^{-1}$; and C–H stretching in the range of $2,800$ – 3000 cm^{-1} . Moreover, there is a sharp feature at 1650 cm^{-1} which most likely can be ascribed to the C=O bond of pure DMF. Therefore, one can conclude that the affinity of MAI toward PbI_2 is higher than that of DMF toward PbI_2 , so the colloidal clusters of perovskite-solvent complexes are formed by the substitution of MAI for DMF. Similar observation and effects were reported in literature.^{30,31} It is

worth mentioning that a small shoulder observed for the band at 1650 cm^{-1} may be ascribed to MAI well-solvated by DMF molecules. This interaction may play an important role in the formation of small colloidal clusters in precursor ink. We further used the as-prepared inks to fabricate perovskite layers on glass substrates using an antisolvent quenching approach. The spin-coating of the perovskite precursor solution involves an antisolvent treatment to facilitate the removal of the host solvent(s) molecules and as a consequence initiate the crystallization of the perovskite film. Several studies have reported the optimal conditions for this step, and it has been shown that antisolvent-solvent interactions, such as dipole-dipole interactions, modulate the dynamics of the process.³² The film morphology is affected by composition-dependent liquid-crystal dynamics and competing crystallization routes that occur during the crucial stages of film formation. To optimize the process, a broad variety of solvents was examined, and it was found that the type of antisolvent used limits the window of operation for morphology and power conversion efficiency (PCE).^{33–36} Therefore, the solvent-engineering technique is critically important for this process. We tried different solvents, along with the use of diverse antisolvents to control the crystallization dynamics and nucleation of the perovskite film. We found that toluene as an antisolvent, together with the DMF/DMSO solvent system allowed us to achieve highly reproducible protocol resulting in extremely uniform, pinhole-free films exhibiting low surface roughness as determined using profilometer and AFM. It is worth emphasizing that these characteristics were obtained for concentrations in the range of 0.008M – 2.5M (**Figure S5**). As we further investigated the thicknesses of thin films using both profilometer and ellipsometry measurements we observed that the relationship between the concentration of precursor ink and thickness of the perovskite film is linear, following the equation:

$$\text{thickness of MAPbI}_3 \text{ film (nm)} = 260 \cdot [\text{concentration of ink (M)}] \quad (1)$$

We further explored the limits of applicability of the method by the preparation of more and more diluted inks. This led us to conclude that using additive-free precursors in DMF:DMSO-toluene solvent-antisolvent system it is possible to control the thickness in the range of 3 nm – 625 nm. The upper limit results from the solubility of MAPbI₃ in the investigated solvent system (2.5M). Importantly, the linear correlation has been preserved in the whole range (**Figure S6**). For further characterization of the ultrathin MAPbI₃ films (below 50 nm) we performed atomic force microscopy (AFM), X-ray diffraction (XRD), and scanning electron microscope (SEM) studies. The SEM and AFM images of the resultant spin-coated below 3 nm MAPbI₃ films on glass substrates are shown in **Figures 2a, 2b, and Figure 2c**.

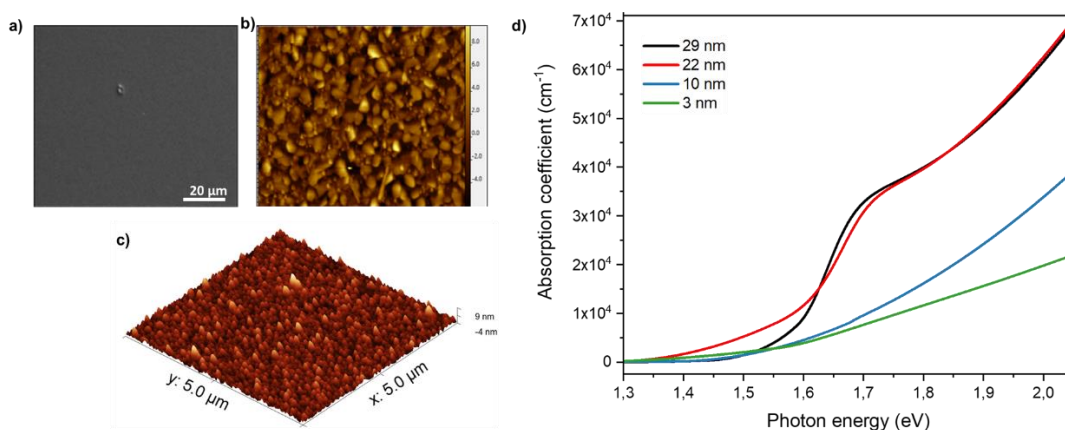


Figure 2. **a)** SEM images of 3 nm MAPI films on a glass substrate. **b-c)** AFM images and RMS roughness values of 3 nm MAPI films on glass **d)** Absorbance spectra of 30, 20, 10, and 3 nm MAPbI₃ films.

The AFM and SEM images both illustrate that the MAPbI₃ layers possess a uniform morphology with a smooth surface, exhibiting a low root mean square (RMS) roughness value of less than 1 nm (additionally, analysis of the thickness and topography of the 3 nm film was presented in the **Supporting Information**, see **Figure S17** and **Figure S18**). However, for thinner films, islands

were observed which can increase for the roughness. These fluctuations in thickness can be attributed to various factors, particularly during the formation of the initial layers. Considering that our film thickness is only a few times larger than the lattice constant of MAPbI₃, that the early stages of crystallization play a significant role in shaping the topography and morphology of the final layer. In these initial stages, perovskite islands begin to grow on the surface. These islands may exhibit a greater affinity for connecting with other perovskite islands rather than the substrate, leading to potential aggregation based on lattice matching. This process likely results in the presence of protruding grains on the surface, thereby contributing to the observed thickness variations. The absorbance spectra of the 30, 20, 10, and 3 nm-thick films are shown in **Figure 2d**. Due to its higher thickness, the 30 and 20-nm perovskite films absorb more light than 10 and 3-nm. For 10 and 3-nm films the absorption coefficient changes substantially. The XRD patterns of the spin-coated MAPbI₃ films on glass substrates are shown in **Figure 3a**. Despite their thicknesses, all the deposited perovskite layers showed high crystallinity reaching an almost excellent tetragonal cell (space group I4cm). In XRD patterns, regardless of the film's thickness, the presence of (110), (220), (310), (224) and (314) diffraction peaks confirm the formation of the tetragonal perovskite structure. Interestingly, we noticed variations in the relative intensity of the (110) peak among the films (**Figure 3a** and **Figure S8**), indicating differences in crystallinity. **Table S1** shows the peak intensity and the peak full-width half maximum (FWHM) of individual crystallite of MAPbI₃ perovskite films measured by the spectral fitting of XRD measurement data as well as the individual crystallite dimensions of the perovskite films, which have been calculated using the Debye - Scherrer equation (**Equation S2**). The peak intensity and individual crystallite dimensions of the perovskite films have been reported in **Table S1**. Notably, an intriguing trend emerges: as the film thickness falls below 200 nm, the crystallite size consistently grows with the

film's thickness. However, once the thickness surpasses 200 nm, it appears that saturation sets in, leading to a stable crystallite size.

In parallel, we performed microstrain analysis on the same XRD patterns (**Figure 3c**) to assess lattice imperfections and structural defects, such as dislocations, stacking faults, and grain boundaries. Line broadening, quantified by FWHM values of diffraction peaks, was employed to estimate both crystallite size and microstrain. This analysis has shown that, in addition to the reduction in crystallite size, there is an increase in microstrain as the film thickness decreases. The microstrain reaches 0.1% for 40 nm, indicating lattice distortion. For films with a thickness of up to 100 nm, the lattice relaxation is observed. The opposite, for the ultrathin layer below 40 nm microstrain reached 2%. That value can be overestimated, it is essential to note that the below 40 nm film exhibited weak peak intensity, which could introduce relatively large errors into the final microstrain value compared to the other samples. This comprehensive characterization sheds light on the crystallinity and microstructural properties of our MAPbI₃ perovskite films, providing valuable insights into their performance and potential applications.

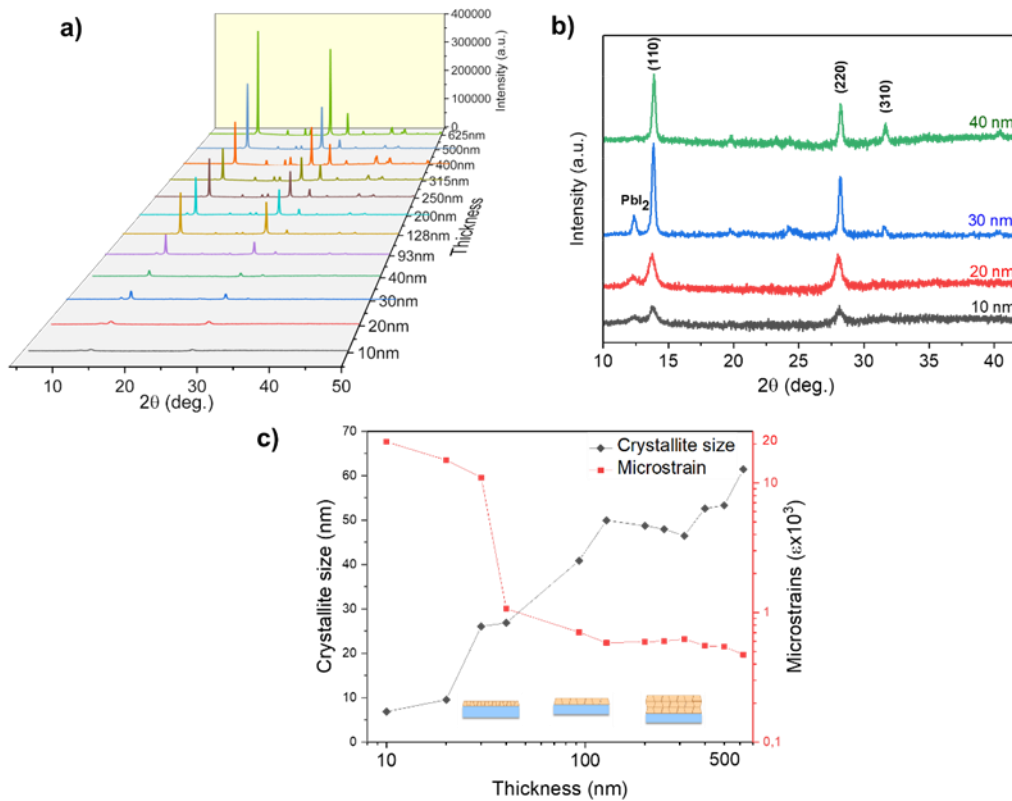


Figure 3. **a)** XRD patterns of the MAPbI₃ perovskite films deposited from various precursor concentrations. **b)** XRD patterns of ultrathin perovskite films. **c)** Calculated microstrain and average crystallite size determined from XRD patterns by performing a Williamson-Hall analysis.

These results are of significant importance as they represent the first-ever structural investigation of ultrathin MAPbI₃ films, ranging from below 30 nanometers down to just a few nanometers in thickness. The reduction in thickness aimed at achieving a high average visible transmittance (AVT) value comes with a trade-off: reduction of effective conversion light to photocurrent. Additionally, we have confirmed that this reduction introduces substantial lattice strains in the MAPbI₃ film. These lattice strains can be attributed to reduced stability and hindered charge transport, as carrier mobility closely correlates with lattice strain.^{37,38} This, in turn, affects the efficiency of carrier collection and may contribute to the formation of defect centers, which can

adversely impact the performance of solar cells.³⁹ Recognizing the potential for overestimating lattice strain in films below 40 nm, we decided to conduct further investigations on solar cell fabrication with two different thicknesses of MAPbI₃. One thickness corresponds to 30 nm, where lattice strains increase dramatically - photovoltaic performance parameters of devices show whether we overestimated lattice strain or not. The second thickness is 10 nm, this aims to explore the feasibility of fabricating functional solar junctions with a photoactive layer at the nanometer scale.

Moreover, for comprehensive and fundamental optical characterization of the spin-coated layers we measured PL using a continuous wave green laser (532 nm, 2.33 eV) as an excitation source. To demonstrate that our fabrication method is reproducible we measured at least 7 spin-coated samples of each thickness in exactly the same measurement conditions (50 μ W exc. power, 300 K, under vacuum).

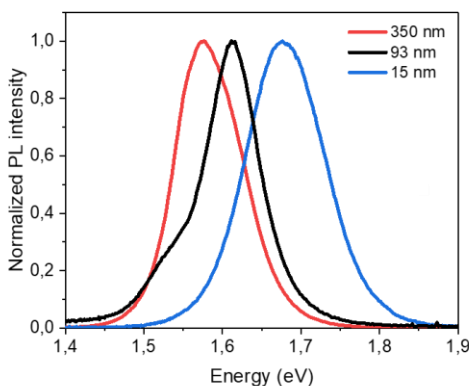


Figure 4. Normalized PL spectra recorded for the samples of different thickness.

The representative spectra are shown in **Figure 4**. The shape of PL and peak position (\sim 1.6 eV) for samples thicker than 225 nm is typical for those reported for MAPbI₃ previously.^{40,41} Interestingly, we observed that the behavior of PL peak was significantly affected by thin film thickness. First of all, the PL is shifted to higher energy with decreasing thickness (**Figure S7**). Of

course, one could expect such a shift in the case of very thin samples (as it can be related to quantum confinement and built-in strain) but here it was clearly observed in the whole investigated thickness range. Another possible explanation is related to the hypothesis that emission in HOIPs such as MAPbI₃ is governed by bistable amphoteric native defects (BANDs), i.e. defects whose nature (donor/acceptor) and formation energy are controlled by the location of Fermi energy.^{42,43} Assuming that due to increased surface to volume ratio in thinner films the concentration of BANDs is higher one can expect such a behavior of PL peak. A further interesting feature in PL spectra is related to the thickness range between 50 nm and 225 nm. Here, the peak is undeniably accompanied by a low-energetic shoulder. The existence of multiple peaks/shoulders in MAPbI₃ spectra was usually reported below phase transition temperature (i.e. 160 K; tetragonal -> orthorhombic) and it was often ascribed to the presence of tetragonal domains in the orthorhombic lattice. Nevertheless, our process does not involve the use of low temperatures. Moreover, XRD patterns did not reveal any signs of different phases and we performed measurements at RT so it is unlikely that the low-energetic shoulder originates from the different phase inclusions. However, this emission may be also related to the contribution of BANDs or different defect states within the bandgap. This hypothesis is quite plausible since we were able to observe PL using below bandgap excitation (787 nm, 1.57 eV). As there was a clear risk that ultrathin MAPbI₃ layers may be more prone to degradation (eventually resulting in the formation of PbI₂) when exposed to ambient air.

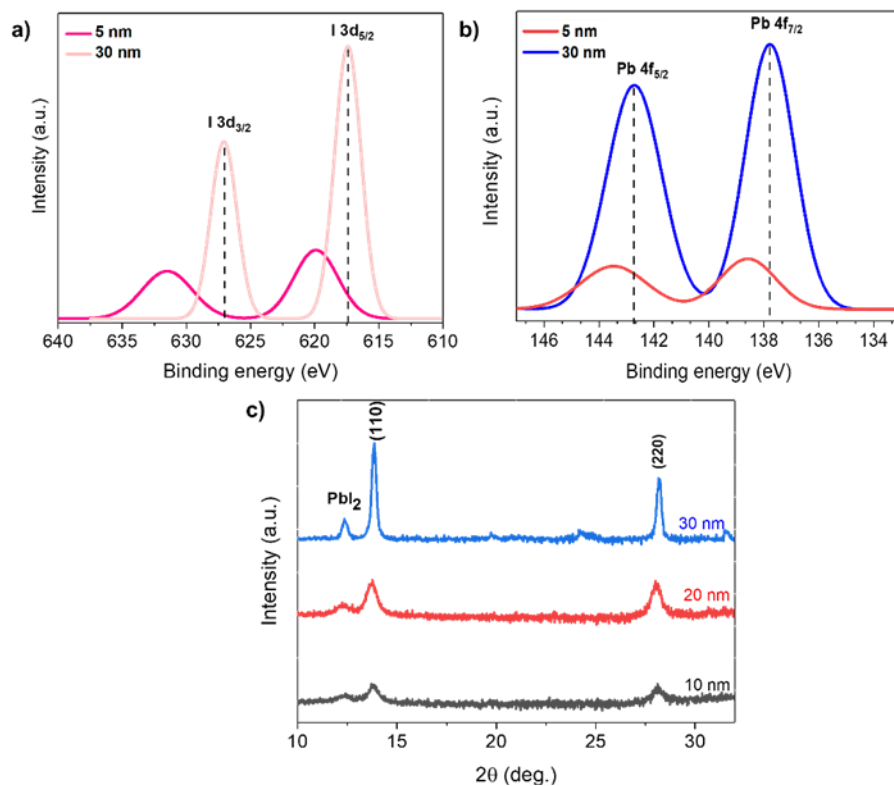


Figure 5. a) XPS spectra of MAPbI₃ 5 and 30 nm films: I 3d. b) XPS spectra of MAPbI₃ 5 and 30 nm films: Pb 4f. c) XRD patterns of ultrathin perovskite films.

That effect was reported in XRD of the ultrathin layer at ambient conditions (**Figure 5c**). That reason, why we used X-ray photoelectron spectroscopy (XPS) to verify if the material is chemically uniform. The spectra shown in **Figures 5a** and **5b** clearly indicate the formation of pure MAPbI₃ for both evaluated ultrathin films (5 nm and 30 nm). The Pb 4f peaks of the 5nm_MAPbI₃ film exhibit higher binding energy compared with 30nm_MAPbI₃. To be specific, **Figure 5a** shows distinguished Pb 4f_{7/2} and Pb4f_{5/2} peaks for 30nm_MAPbI₃ at 137.7 and 142.7 eV, respectively. The corresponding Pb peaks of 5nm_MAPbI₃ were shifted to a higher binding energy of 138.6 eV for Pb4f_{7/2} and 143.5 eV for Pb4f_{5/2}, which could be attributed to the changed

chemical environment. Note that both the distinguished I3d_{5/2} (619.9 eV) and I3d_{3/2} (631.5 eV) peaks for 5nm_MAPbI₃ are also shifted toward higher binding energy compared to those of the 30nm_MAPbI₃ film (617.5 eV and 627.1 eV) (**Figure 5b**). This shift suggests a change in the chemical environment of the [PbI₆]⁴⁻ octahedron, probably deformation of complex arrangement with decreasing dimensionality.

Finally, encouraged by the results obtained for ultra-thin films we fabricated flexible semi-transparent PSCs with planar architecture and inverted configuration (p-i-n), (active area of 1 cm²) using the diluted, additive-free inks on flex substrate with the following structure PET/indium zinc oxide (IZO)/PEDOT:PSS/MAPbI₃/C60/bathocuproine (BCP)/Ag (**Figure 7a**). Here, it is worth noting that in general fabrication of top electrodes for semi-transparent PSCs is a separate, yet very important, issue being the subject of numerous studies. Among many approaches, the most common are: direct deposition of transparent conductive oxides-based top electrodes without protective buffer layers, fabrication of three-dimensional amorphous ITO (a-ITO)/Ag mesh directly on semi-transparent perovskite solar cells, and using a dielectric/metal/dielectric (DMD) multilayer film as the top transparent electrode.⁴⁴ Continuing the idea of a simple approach, we decided to deposit just 10 nm of silver layer without any additional anti-reflective coatings. AVT (between 300 and 900 nm spectral region) for the evaluated PSCs was calculated using the formula⁴⁵

$$AVT = \frac{\int_{300}^{900} I(\lambda)T(\lambda)d\lambda}{\int_{300}^{900} I(\lambda)d\lambda} \quad (2)$$

where I(λ) is the photon flux under AM 1.5G illumination and T(λ) is the photopic response of the human eyes. We achieved a current density (J_{sc}) of 8.68 mA/cm² and combined with an open-circuit voltage (V_{oc}) of 0.92 V, and fill-factor (FF) of 71.5% this resulted in a PCE of 5.7% for the champion device under AM 1.5G irradiation (**Figure 6b**, **Figure 7a** and **Figure S19**). The

champion device combining high performance and good transparency (AVT of 21.5%) was obtained for PSC consisting of a 30 nm MAPbI₃ layer and 10 nm of Ag (**Figure 6c**). The digital photograph of the corresponding device in **Figure 6d** depicts the overall optical transparency and color neutrality. We also tried to fabricate PSC with the thinnest ever MAPbI₃ layer, 10 nm. An impressive PSC with PCE of 1.9% an AVT of 41.1% (62.9% without Ag electrode) is achieved when the active layer reaches only 10 nm of thickness (**Figure 6b** and **6c**). These devices also demonstrate high reproducibility with an average efficiency of $1.8 \pm 0.1\%$, as shown in **Figure 6b**.

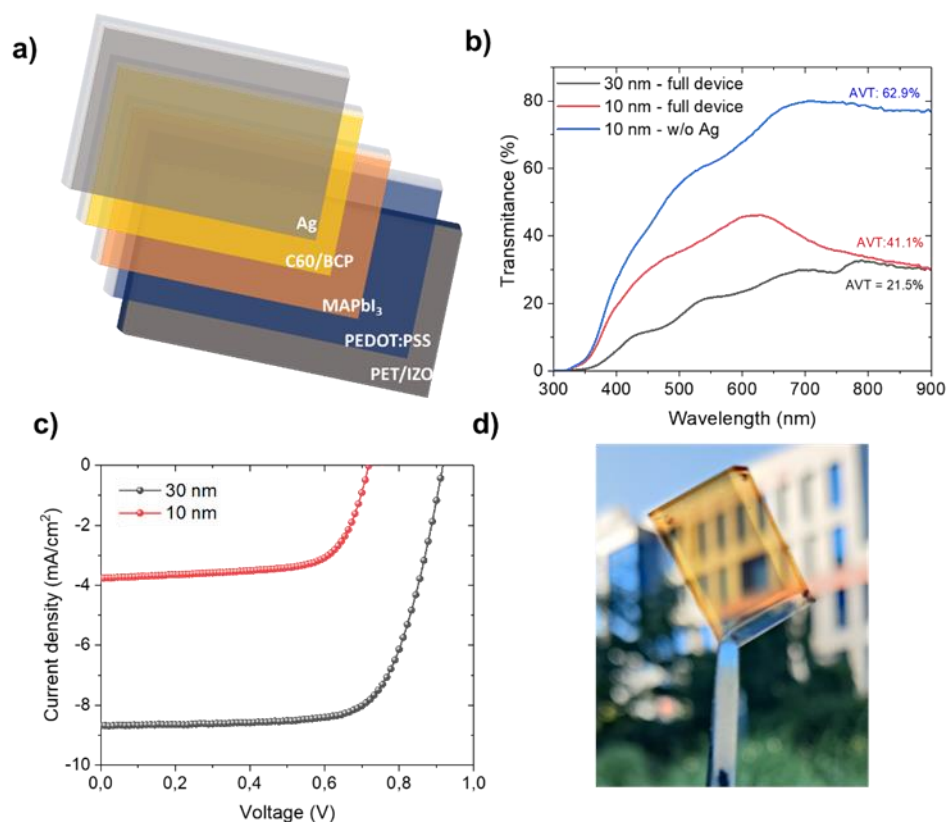


Figure 6. **a)** Device configuration of PET/IZO-based semi-transparent PSCs fabricated in this work **b)** J-V curves for the optimized perovskite solar cells fabricated with 10 and 30 nm of MAPbI₃ layer. **c)** Transmittance spectra of the active layer of such cells. **d)** Photograph through a typical flexible semi-transparent perovskite solar cell with 30 nm of MAPbI₃ layer and 10 nm silver electrode, demonstrating neutral color and semitransparency.

As a common trend in all of these devices, a gradual decrease in the J_{sc} with decreasing perovskite layer thickness is observed due to reduced photon absorption, especially when the active layer was reduced to 10 nm. This trend is also reflected in the overall PCEs of the completed devices. Notably, the decrease is more rapid for the 10 nm_MAPbI₃ devices than that of the 30 nm_MAPbI₃ ones as a combined result of a significant decrease in FF, V_{oc} , and J_{sc} . This is consistent with the fact that the fabrication of perovskite films below 10 nm of thickness formed film with high lattice strain (up to 2%). Probably, fabrication of that type of ultrathin film on a more thick PEDOT:PSS with high roughness of the surface leads to more defects at PEDOT:PSS/MAPbI₃ interlayer. Nevertheless, PEDOT:PSS layer has good uniformity without any pinholes as seen in the SEM images (**Figure 7c**). In summary, 30nm_MAPbI₃ PSC is the technical limit for minimizing the thickness of the active layer. Further decreasing thickness affected with increasing lattice strains and decrease of absorption coefficient, so drastically dropped all device performance parameters. To ensure the reliability and performance of the manufactured perovskite solar cells (PSCs), we conducted stability assessments by measuring the stabilized power output in proximity to the maximum power point (MPP). When measuring the photocurrent precisely at the MPP under continuous AM 1.5G illumination, the performance of the fabricated semi-transparent PSCs exhibited excellent stability.

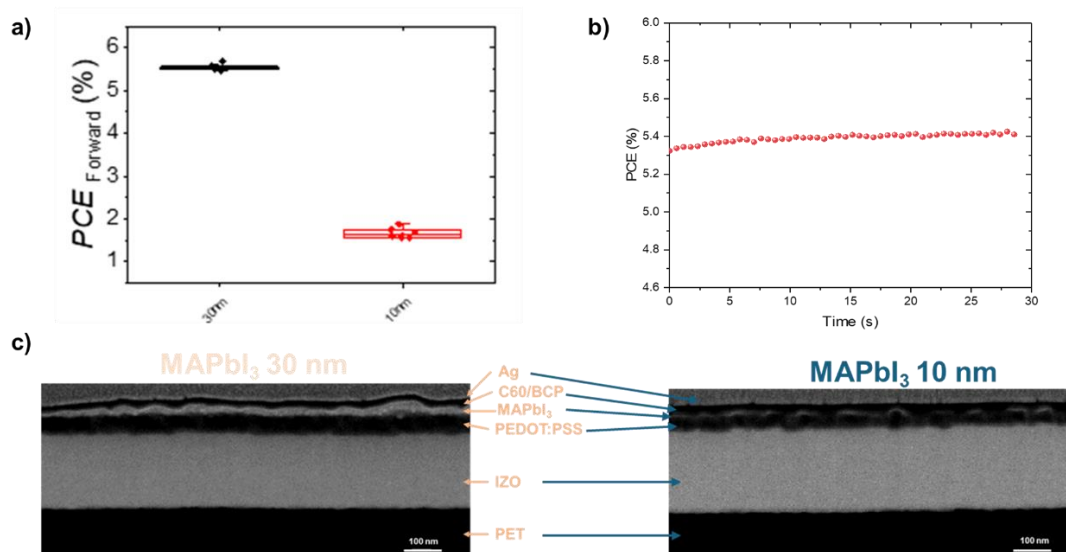


Figure 7. **a)** Statistic of the photovoltaic performance measured for the perovskite solar cells with different MAPbI₃ thickness: 10 (red) and 30 nm (black). **b)** A typical stabilized PCE of PSC is determined by measuring the photocurrent at the maximum power point (MPP) under continuous AM 1.5G irradiation. **c)** FIB-SEM image of the best-performing ultrathin solar cells.

CONCLUSIONS

We developed a simple, yet elegant, protocol using solvent engineering for the deposition of extremely uniform and ultra-thin perovskite layers. Probably, the high reproducibility and the ability to control a wide range of molar concentrations were made possible through the stabilization of an intermediate phase using a precisely formulated precursor solution realized *via* chemistry precursor solution. Starting from high-purity additive-free materials we were able to control the thickness of uniform MAPbI₃ film in a range of 3 nm – 625 nm. These results will provide an effective strategy for the fabrication of uniform semi-transparent perovskite solar cells based on ultra-thin MAPbI₃, demonstrated 5.7% PCE under standard conditions (AM 1.5 G radiation, 100 mW cm⁻²) for 30nm_MaPbI₃-based cells. Remarkably, we achieved 1.9% of PCE for 10 nm_MAPbI₃. These results represent a key advancement for producing ultra-lightweight,

highly transparent devices with reduced lead content—a significant leap toward sustainability. Our findings also illuminate a promising path for continued research in this field, promising further innovation and development in the future.

ASSOCIATED CONTENT

Supporting Information: experimental details, NMR spectra of MAI, optical absorption spectra for samples of different thickness, relationship between ink concentration and film thickness, PL peak position as a function of film thickness, Scherrer and Williamson – Hall analyses of XRD patterns, SEM images, additional J-V curves, EQE for 10 nm and 30 nm MAPbI₃ layers

AUTHOR INFORMATION

Corresponding Author

*lukasz.przypis@pwr.edu.pl

Author Contributions

The manuscript was written through contributions of all authors. All authors have given approval to the final version of the manuscript. ‡These authors contributed equally.

ACKNOWLEDGMENT

This work was supported by Polish National Science Centre (NCN) Opus Grant UMO-2019/33/B/ST3/03021. The authors would like to acknowledge the contributions and scientific assistance of the late Prof. Wlodek Walukiewicz

REFERENCES

- (1) Stranks, S. D.; Eperon, G. E.; Grancini, G.; Menelaou, C.; Alcocer, M. J. P.; Leijtens, T.; Herz, L. M.; Petrozza, A.; Snaith, H. J. Electron-Hole Diffusion Lengths Exceeding 1

- Micrometer in an Organometal Trihalide Perovskite Absorber. *Science (1979)* **2013**, 342 (6156), 341–344. <https://doi.org/10.1126/science.1243982>.
- (2) Zhumekenov, A. A.; Saidaminov, M. I.; Haque, M. A.; Alarousu, E.; Sarmah, S. P.; Murali, B.; Dursun, I.; Miao, X. H.; Abdelhady, A. L.; Wu, T.; Mohammed, O. F.; Bakr, O. M. Formamidinium Lead Halide Perovskite Crystals with Unprecedented Long Carrier Dynamics and Diffusion Length. *ACS Energy Lett* **2016**, 1 (1), 32–37. <https://doi.org/10.1021/acsenergylett.6b00002>.
 - (3) Chang, Y. H.; Park, C. H. First-Principles Study of the Structural and the Electronic Properties of the Lead-Halide-Based Inorganic-Organic Perovskites (CH₃NH₃)PbX₃ and CsPbX₃ (X = Cl, Br, I). *Journal of the Korean Physical Society* **2004**, 44 (4), 889–893.
 - (4) Kulkarni, S. A.; Baikie, T.; Boix, P. P.; Yantara, N.; Mathews, N.; Mhaisalkar, S. Band-Gap Tuning of Lead Halide Perovskites Using a Sequential Deposition Process. *J Mater Chem A Mater* **2014**, 2 (24), 9221–9225. <https://doi.org/10.1039/c4ta00435c>.
 - (5) Żuraw, W.; Vinocour Pacheco, F. A.; Sánchez-Díaz, J.; Przypis, Ł.; Mejía Escobar, M. A.; Almosni, S.; Vescio, G.; Martínez-Pastor, J. P.; Garrido, B.; Kudrawiec, R.; Mora-Seró, I.; Öz, S. Large-Area, Flexible, Lead-Free Sn-Perovskite Solar Modules. *ACS Energy Lett* **2023**, 8 (11), 4885–4887. <https://doi.org/10.1021/acsenergylett.3c02066>.
 - (6) <https://www.nrel.gov/pv/assets/pdfs/best-research-cell-eFFiciencies-rev211214.pdf> (accessed: May 2023).
 - (7) Yue, W.; Yang, H.; Cai, H.; Xiong, Y.; Zhou, T.; Liu, Y.; Zhao, J.; Huang, F.; Cheng, Y.; Zhong, J. Printable High-efficiency and Stable FAPbBr₃ Perovskite Solar Cells for Multifunctional Building-integrated Photovoltaics. *Advanced Materials* **2023**, 2301548, 1–11. <https://doi.org/10.1002/adma.202301548>.
 - (8) Hörantner, M. T.; Nayak, P. K.; Mukhopadhyay, S.; Wojciechowski, K.; Beck, C.; McMeekin, D.; Kamino, B.; Eperon, G. E.; Snaith, H. J. Shunt-Blocking Layers for Semitransparent Perovskite Solar Cells. *Adv Mater Interfaces* **2016**, 3 (10), 1–7. <https://doi.org/10.1002/admi.201500837>.
 - (9) Cannavale, A.; Eperon, G. E.; Cossari, P.; Abate, A.; Snaith, H. J.; Gigli, G. Perovskite Photovoltachromic Cells for Building Integration. *Energy Environ Sci* **2015**, 8 (5), 1578–1584. <https://doi.org/10.1039/c5ee00896d>.
 - (10) Martín-Chivelet, N.; Kapsis, K.; Wilson, H. R.; Delisle, V.; Yang, R.; Olivieri, L.; Polo, J.; Eisenlohr, J.; Roy, B.; Maturi, L.; Otnes, G.; Dallapiccola, M.; Upalakshi Wijeratne, W. M. P. Building-Integrated Photovoltaic (BIPV) Products and Systems: A Review of Energy-Related Behavior. *Energy Build* **2022**, 262, 111998. <https://doi.org/10.1016/J.ENBUILD.2022.111998>.
 - (11) Huang, J.; Yuan, Y.; Shao, Y.; Yan, Y. Understanding the Physical Properties of Hybrid Perovskites for Photovoltaic Applications. **2017**. <https://doi.org/10.1038/natrevmats.2017.42>.

- (12) Bag, S.; Durstock, M. F. Efficient Semi-Transparent Planar Perovskite Solar Cells Using a ‘Molecular Glue.’ *Nano Energy* **2016**, *30* (October), 542–548. <https://doi.org/10.1016/j.nanoen.2016.10.044>.
- (13) Marques, A. S.; Faria, R. M.; Freitas, J. N.; Nogueira, A. F. Low-Temperature Blade-Coated Perovskite Solar Cells. *Ind Eng Chem Res* **2021**, *60* (19), 7145–7154. <https://doi.org/10.1021/acs.iecr.1c00789>.
- (14) Bae, I. G.; Park, B. All-Self-Metered Solution-Coating Process in Ambient Air for the Fabrication of Efficient, Large-Area, and Semitransparent Perovskite Solar Cells. *Sustain Energy Fuels* **2020**, *4* (6), 3115–3128. <https://doi.org/10.1039/d0se00598c>.
- (15) Rahmany, S.; Etgar, L. Semitransparent Perovskite Solar Cells. *ACS Energy Lett* **2020**, *5*, 1519–1531. <https://doi.org/10.1021/acseenergylett.0c00417>.
- (16) Eperon, G. E.; Burlakov, V. M.; Goriely, A.; Snaith, H. J. Neutral Color Semitransparent Microstructured Perovskite Solar Cells. *ACS Nano* **2014**, *8* (1), 591–598. <https://doi.org/10.1021/nn4052309>.
- (17) Eperon, G. E.; Bryant, D.; Troughton, J.; Stranks, S. D.; Johnston, M. B.; Watson, T.; Worsley, D. A.; Snaith, H. J. Efficient, Semitransparent Neutral-Colored Solar Cells Based on Microstructured Formamidinium Lead Trihalide Perovskite. *Journal of Physical Chemistry Letters* **2015**, *6* (1), 129–138. <https://doi.org/10.1021/jz502367k>.
- (18) Rahmany, S.; Layani, M.; Magdassi, S.; Etgar, L. Fully Functional Semi-Transparent Perovskite Solar Cell Fabricated in Ambient Air. *Sustain Energy Fuels* **2017**, *1* (10), 2120–2127. <https://doi.org/10.1039/c7se00383h>.
- (19) Aharon, S.; Layani, M.; Cohen, B. El; Shukrun, E.; Magdassi, S.; Etgar, L. Self-Assembly of Perovskite for Fabrication of Semitransparent Perovskite Solar Cells. *Adv Mater Interfaces* **2015**, *2* (12), 1–6. <https://doi.org/10.1002/admi.201500118>.
- (20) Zhang, Z.; Ji, R.; Jia, X.; Wang, S. J.; Deconinck, M.; Siliavka, E.; Vaynzof, Y. Semitransparent Perovskite Solar Cells with an Evaporated Ultra-Thin Perovskite Absorber. *Adv Funct Mater* **2023**. <https://doi.org/10.1002/adfm.202307471>.
- (21) Kwon, H. C.; Kim, A.; Lee, H.; Lee, D.; Jeong, S.; Moon, J. Parallelized Nanopillar Perovskites for Semitransparent Solar Cells Using an Anodized Aluminum Oxide Scaffold. *Adv Energy Mater* **2016**, *6* (20). <https://doi.org/10.1002/aenm.201601055>.
- (22) Della Gaspera, E.; Peng, Y.; Hou, Q.; Spiccia, L.; Bach, U.; Jasieniak, J. J.; Cheng, Y. B. Ultra-Thin High Efficiency Semitransparent Perovskite Solar Cells. *Nano Energy* **2015**, *13*, 249–257. <https://doi.org/10.1016/j.nanoen.2015.02.028>.
- (23) Zhang, Z.; Ji, R.; Jia, X.; Wang, S. J.; Deconinck, M.; Siliavka, E.; Vaynzof, Y. Semitransparent Perovskite Solar Cells with an Evaporated Ultra-Thin Perovskite Absorber. *Adv Funct Mater* **2023**. <https://doi.org/10.1002/adfm.202307471>.
- (24) Paliwal, A.; Mardegan, L.; Roldan-Carmona, C.; Palazon, F.; Liu, T. Y.; Bolink, H. J. Efficient Semitransparent Perovskite Solar Cells Based on Thin Compact Vacuum

- Deposited CH₃NH₃PbI₃ Films. *Adv Mater Interfaces* **2022**, *9* (29). <https://doi.org/10.1002/admi.202201222>.
- (25) Roldán-Carmona, C.; Malinkiewicz, O.; Betancur, R.; Longo, G.; Momblona, C.; Jaramillo, F.; Camacho, L.; Bolink, H. J. High Efficiency Single-Junction Semitransparent Perovskite Solar Cells. *Energy Environ Sci* **2014**, *7* (9), 2968–2973. <https://doi.org/10.1039/c4ee01389a>.
- (26) Tisdale, J. T.; Smith, T.; Salasin, J. R.; Ahmadi, M.; Johnson, N.; Ievlev, A. V.; Koehler, M.; Rawn, C. J.; Lukosi, E.; Hu, B. Precursor Purity Effects on Solution-Based Growth of MAPbBr₃ Single Crystals towards Efficient Radiation Sensing. *CrystEngComm* **2018**, *20* (48), 7818–7825. <https://doi.org/10.1039/c8ce01498a>.
- (27) Dasgupta, S.; Misztal, K.; Fuentes Pineda, R.; Mróz, W.; Pawlaczyk, Ł.; Serafińczuk, J.; Barker, A. J.; Ahmad, T.; Herman, A. P.; Sahayaraj, S.; Kudrawiec, R.; Petrozza, A.; Dudkowiak, A.; Wojciechowski, K. New Synthetic Route of Ultra-Pure Alkylammonium Iodides for Perovskite Thin Films of Superior Optoelectronic Properties. *Energy Technology* **2020**, *n/a* (n/a). <https://doi.org/10.1002/ente.202000478>.
- (28) Mcmeehin, D. P.; Wang, Z.; Rehman, W.; Pulvirenti, F.; Patel, J. B.; Noel, N. K.; Johnston, M. B.; Marder, S. R.; Herz, L. M.; Snaith, H. J. Crystallization Kinetics and Morphology Control of Formamidinium – Cesium Mixed-Cation Lead Mixed-Halide Perovskite via Tunability of the Colloidal Precursor Solution. **2017**. <https://doi.org/10.1002/adma.201607039>.
- (29) Ran, C.; Gao, W.; Li, N.; Xia, Y.; Li, Q.; Wu, Z.; Zhou, H.; Chen, Y.; Wang, M.; Huang, W. Facet-Dependent Control of PbI₂ Colloids for over 20% Efficient Perovskite Solar Cells. *ACS Energy Lett* **2019**, *4* (1), 358–367. <https://doi.org/10.1021/acsenenergylett.8b02262>.
- (30) Li, B.; Li, M.; Fei, C.; Cao, G.; Tian, J. Colloidal Engineering for Monolayer CH₃NH₃PbI₃ Films toward High Performance Perovskite Solar Cells. *J Mater Chem A Mater* **2017**, *5* (46), 24168–24177. <https://doi.org/10.1039/c7ta08761f>.
- (31) Yang, J.; Hu, J.; Zhang, W.; Han, H.; Chen, Y.; Hu, Y. The Opportunities and Challenges of Ionic Liquids in Perovskite Solar Cells. *Journal of Energy Chemistry*. Elsevier B.V. February 1, 2023, pp 157–171. <https://doi.org/10.1016/j.jechem.2022.10.048>.
- (32) Bautista-quijano, J. R.; Vaynzof, Y.; Telschow, O.; Paulus, F.; Bautista-, J. R. Solvent – Antisolvent Interactions in Metal Halide Perovskites. **2023**, 10588–10603. <https://doi.org/10.1039/d3cc02090h>.
- (33) Taylor, A. D.; Sun, Q.; Goetz, K. P.; An, Q.; Schramm, T.; Hofstetter, Y.; Litterst, M.; Paulus, F.; Vaynzof, Y. A General Approach to High-Efficiency Perovskite Solar Cells by Any Antisolvent. *Nat Commun* **2021**, *12* (1), 1–11. <https://doi.org/10.1038/s41467-021-22049-8>.

- (34) Jeon, N. J.; Noh, J. H.; Kim, Y. C.; Yang, W. S.; Ryu, S.; Seok, S. Il. Solvent Engineering for High-Performance Inorganic-Organic Hybrid Perovskite Solar Cells. *Nat Mater* **2014**, *13* (9), 897–903. <https://doi.org/10.1038/nmat4014>.
- (35) Zhang, W.; Li, Y.; Liu, X.; Tang, D.; Li, X.; Yuan, X. Ethyl Acetate Green Antisolvent Process for High-Performance Planar Low-Temperature SnO₂-Based Perovskite Solar Cells Made in Ambient Air. *Chemical Engineering Journal* **2020**, *379* (July 2019), 122298. <https://doi.org/10.1016/j.cej.2019.122298>.
- (36) Yang, F.; Kapil, G.; Zhang, P.; Hu, Z.; Kamarudin, M. A.; Ma, T.; Hayase, S. Dependence of Acetate-Based Antisolvents for High Humidity Fabrication of CH₃NH₃PbI₃ Perovskite Devices in Ambient Atmosphere. *ACS Appl Mater Interfaces* **2018**, *10* (19), 16482–16489. <https://doi.org/10.1021/acsami.8b02554>.
- (37) Nishimura, K.; Hirotsu, D.; Kamarudin, M. A.; Shen, Q.; Toyoda, T.; Iikubo, S.; Minemoto, T.; Yoshino, K.; Hayase, S. Relationship between Lattice Strain and Efficiency for Sn-Perovskite Solar Cells. *ACS Appl Mater Interfaces* **2019**, *11* (34), 31105–31110. <https://doi.org/10.1021/acsami.9b09564>.
- (38) Zhu, C.; Niu, X.; Fu, Y.; Li, N.; Hu, C.; Chen, Y.; He, X.; Na, G.; Liu, P.; Zai, H.; Ge, Y.; Lu, Y.; Ke, X.; Bai, Y.; Yang, S.; Chen, P.; Li, Y.; Sui, M.; Zhang, L.; Zhou, H.; Chen, Q. Strain Engineering in Perovskite Solar Cells and Its Impacts on Carrier Dynamics. *Nat Commun* **2019**, *10* (1). <https://doi.org/10.1038/s41467-019-08507-4>.
- (39) Fang, J.; Ding, Z.; Chang, X.; Lu, J.; Yang, T.; Wen, J.; Fan, Y.; Zhang, Y.; Luo, T.; Chen, Y.; Liu, S. (Frank); Zhao, K. Microstructure and Lattice Strain Control towards High-Performance Ambient Green-Printed Perovskite Solar Cells. *J Mater Chem A Mater* **2021**, *9* (22), 13297–13305. <https://doi.org/10.1039/d1ta01763b>.
- (40) D’Innocenzo, V.; Srimath Kandada, A. R.; De Bastiani, M.; Gandini, M.; Petrozza, A. Tuning the Light Emission Properties by Band Gap Engineering in Hybrid Lead Halide Perovskite. *J Am Chem Soc* **2014**, *136* (51), 17730–17733. <https://doi.org/10.1021/ja511198f>.
- (41) Staub, F.; Anusca, I.; Lupascu, D. C.; Rau, U.; Kirchartz, T. Effect of Reabsorption and Photon Recycling on Photoluminescence Spectra and Transients in Lead-Halide Perovskite Crystals. *J Phys Materials* **2020**, *3* (2). <https://doi.org/10.1088/2515-7639/ab6fd0>.
- (42) Walukiewicz, W.; Wang, S.; Wu, X.; Sherburne, M. P.; Ager, J. W.; Asta, M. D. Photophysics of Localized Deep Defect States in Hybrid Organic-Inorganic Perovskites. *Journal of Physical Chemistry C* **2021**, *125* (12), 6975–6982. <https://doi.org/10.1021/acs.jpcc.1c01150>.
- (43) Walukiewicz, W.; Wang, S.; Wu, X.; Li, R.; Sherburne, M. P.; Wu, B.; Sum, T. C.; Ager, J. W.; Asta, M. D. The Bright Side and Dark Side of Hybrid Organic-Inorganic Perovskites. *Journal of Physical Chemistry C* **2020**, *124* (50), 27340–27355. <https://doi.org/10.1021/acs.jpcc.0c08263>.

- (44) Zaroni, K. P. S.; Paliwal, A.; Hernández-Fenollosa, M. A.; Repecaud, P. A.; Morales-Masis, M.; Bolink, H. J. ITO Top-Electrodes via Industrial-Scale PLD for Efficient Buffer-Layer-Free Semitransparent Perovskite Solar Cells. *Adv Mater Technol* **2022**, 7 (10). <https://doi.org/10.1002/admt.202101747>.
- (45) Yang, C.; Liu, D.; Bates, M.; Barr, M. C.; Lunt, R. R. How to Accurately Report Transparent Solar Cells. *Joule*. Cell Press August 21, 2019, pp 1803–1809. <https://doi.org/10.1016/j.joule.2019.06.005>.

TOC GRAPHICS

